Front. Earth Sci. 2016, 10(2): 195–204
DOI 10.1007/s11707-015-0509-4

RESEARCH ARTICLE

Detection of radio-frequency interference signals from AMSR-E data over the United States with snow cover

Chengcheng FENG[1], Xiaolei ZOU (✉)[2], Juan ZHAO[3]

1 Center of Data Assimilation for Research and Application, Nanjing University of Information Science & Technology, Nanjing 210044, China
2 Earth System Science Interdisciplinary Center, University of Maryland, College Park, MD 20740-3823, USA
3 China Meteorological Administration Training Centre, Beijing 100081, China

Abstract Radio Frequency Interference (RFI) causes severe contamination to passive and active microwave sensing observations and corresponding retrieval products. RFI signals should be detected and filtered before applying the microwave data to retrieval and data assimilation. It is difficult to detect RFI over land surfaces covered by snow because of the scattering effect of snow surface. The double principal component analysis (DPCA) method is adopted in this study, and its ability in identifying RFI signals in AMSR-E data over snow covered regions is investigated. Results show that the DPCA method can detect RFI signals effectively in spite of the impact of snow scattering, and the detected RFI signals persistent over time. Compared to other methods, such as PCA and normalized PCA, DPCA is more robust and suitable for operational application.

Keywords Radio Frequency Interference (RFI), AMSR-E, double principal component analysis (DPCA)

1 Introduction

The Advanced Microwave Scanning Radiometer on the Earth Observing System (AMSR-E) (Kawanishi et al., 2003) on board the Aqua satellite (Parkinson et al., 2003) was launched by the National Aeronautics and Space Administration (NASA) on May 4, 2002. AMSR-E design was modified from that of AMSR (Imaoka et al., 2002), which flew with the Japanese ADEOS-II. AMSR-E receives the microwave emissions from the Earth's surface and atmosphere. Due to its advantage of all-day observation, penetrability, and all-weather coverage, AMSR-E measurements have been widely used in the research of global environmental change.

From the AMSR-E measurements, we can retrieve the surface wind speed, atmospheric total cloud liquid water content, water vapor, precipitation, soil moisture, vegetation parameter, surface temperature, and snow cover, etc. (Njoku and Li, 1999; Njoku et al., 2000, 2003; Owe et al., 2001; Kelly et al., 2003; Wilheit et al., 2003). The AMSR-E data record is very important in climate change monitoring and data assimilation in numerical weather prediction, but man-made radiative signals are also received by the microwave instrument and interfere with the natural Earth's thermal emission. This phenomenon, satellite observations being mixed with signals from active microwave transmitters, is referred to as Radio-Frequency Interference (RFI). There are many possible sources of RFI, including radar, air traffic control, cell phones, garage door remote controls, GPS signals on highways, defense tracking, vehicle speed detection for law enforcement, etc. (Zhao et al., 2013).

Previous studies of AMSR-E and WindSat data show that RFI signals over land often appear at low frequencies such as C-band and X-band (Li et al., 2004; Njoku et al., 2005; Ellingson and Johnson, 2006; McKague et al., 2010; Wu and Weng, 2011; Lacava et al., 2013). In the United States, RFI signals often appear at C-band. For Europe, RFI occurs at X-band. For Japan, there are RFI signals at both C-band and X-band. The presence of RFI signals will reduce the scientific value of satellite measurements. For instance, the AMSR-E 6.925 GHz channel has been removed in the retrieval of soil moisture over land because of the presence of RFI (Li et al., 2004). Therefore, it is of great importance to identify the RFI signals and remove them prior to applying the data to retrieval and data assimilation.

To detect the RFI signals, many methods have been used, such as the spectral difference method (Li et al.,

Received March 14, 2014; accepted December 1, 2014

E-mail: xzou@nuist.edu.cn

2004), the mean/standard deviation method (Njoku et al., 2005), and the Principal Component Analysis (PCA) (Li et al., 2006). Zou et al. (2012) also introduced the normalized PCA (NPCA) method to detect RFI in FY-3B MWRI (MicroWave Radiation Imager) data over snow-covered surfaces in winter. Zhao et al. (2013) developed a double Principal Component Analysis (DPCA) method for RFI identification in WindSat data over Greenland and Antarctic where the RFI signals are distributed in coastal areas with permanent frozen ice surfaces away from the coast. However, how to identify RFI over the snow-scattering surface is still an open issue. This study attempts to apply the DPCA method to detect RFI signals over the United States with snow cover during a snowstorm process in winter. The paper is organized as follows. Section 2 provides a brief description of AMSR-E data. Section 3 introduces the DPCA method in detail. Numerical results are presented in Section 4. Section 5 gives some conclusions.

2 AMSR-E Data Description

AMSR-E is a passive-microwave radiometer system which has twelve channels and six frequencies. It measures the brightness temperatures at 6.925 GHz, 10.65 GHz, 18.7 GHz, 23.8 GHz, 36.5 GHz, and 89.0 GHz on horizontal and vertical polarization (Parkinson et al., 2003). AMSR-E is being flown in a sun-synchronous orbit at an altitude of 705 km with an observational swath width of 1,445 km. The antenna of AMSR-E conically scans the earth at a 47.4° angle which corresponds to a local earth incidence angle of 55°. This satellite spans the equator twice a day at approximately 13:30 and 1:30 local solar time. The parameters and characteristics of the radiometer are listed in Table 1 (Njoku et al., 2005).

There are several levels of AMSR-E standard products. The AMSR-E Lever-1A product contains scene counts with radiometric and geometric information. Level-1B data contains the brightness temperatures converted from antenna temperature. The AMSR-E antenna gain patterns are reconstructed at each channel to five footprints at the resolutions of 56 km, 38 km, 21 km, 12 km, and 5.4 km (Ashcroft and Wentz, 2000). After calibration and re-sampling, Level-2A brightness temperatures are produced from Level-1B data by the Remote Sensing System (RSS). The higher-resolution channels are resampled to correspond to the footprint sizes of the lower-resolution channels. This ensures that the observations at different frequencies describe identical locations. The resulting brightness temperatures are called effective observations in contrast to the original or actual observations. The calibrated Level-2A brightness temperatures can be used as the basis for the higher-level geophysical processing of Level-2B and Level-3 data products (Shibata et al., 2003). In this study, Level-2A AMSR-E brightness temperatures from October 2010 to July 2011 are used and are binned onto a 1/3 degrees by 1/3 degrees latitudinal and longitudinal grid over the United States. Here, 1/3 degrees spatial resolution is selected subjectively. The Level-2A data can also be binned onto other different resolutions, and the results show that the spatial resolution of the grid hardly affects the distribution of detected RFI (figure omitted).

3 DPCA method

RFI signals are often directional and narrow-banded, being isolated in space and persistent in time. Different from RFI signals, the radiation from earth's surface is smooth and ultra-wideband. The multi-channel correlations of radiation data from natural radiation are usually high, but RFI at the low frequency can reduce the channel-by-channel correlation.

The double principal component analysis method (DPCA) developed by Zhao et al. (2013) has been used to identify RFI in the WindSat data over Greenland and Antarctic. This method takes advantage of the de-correlation for RFI signals and the correlation characteristics of radiation data in different channels for natural surfaces including snow cover.

The DPCA method consists of two steps: In the first step, we chose the AMSR-E brightness temperatures at ten low frequency channels (except 89.0 GHz) to make a ten-component vector in each grid (1/3 degrees latitudinal and longitudinal resolution).

The vector is defined as

$$\vec{V}_i = \begin{pmatrix} TB_{6.9\mathrm{H},i} \\ TB_{6.9\mathrm{V},i} \\ TB_{10.7\mathrm{H},i} \\ TB_{10.7\mathrm{V},i} \\ TB_{18.7\mathrm{H},i} \\ TB_{18.7\mathrm{V},i} \\ TB_{23.8\mathrm{H},i} \\ TB_{23.8\mathrm{V},i} \\ TB_{36.5\mathrm{H},i} \\ TB_{36.5\mathrm{V},i} \end{pmatrix}, \; i = 1,2,...,N, \tag{1}$$

where N is the total number of data points over the research region. 6.925, 10.65, 18.7, 23.8, and 36.5 refer to the frequency of channels. H is horizontal polarization, and V is vertical polarization.

The data matrix for PCA of $\vec{V}_i$ is defined as

Table 1 AMSR-E instrument characteristics

Characteristics	6.9H/V	10.7H/V	18.7H/V	23.8H/V	36.5H/V	89.0H/V
Center frequency/GHz	6.925	10.65	18.7	23.8	36.5	89.0
Bandwidth/MHz	350	100	200	400	1,000	3,000
Sensitivity/K	0.3	0.6	0.6	0.6	0.6	1.1
IFOV/km	75×43	51×29	27×16	32×18	14×8	6×4
Sample spacing/km	10×10	10×10	10×10	10×10	10×10	6×4
Integration time/ms	2.5	2.5	2.5	2.5	2.5	1.2
Main-beam efficiency/%	95.1	94.8	95.8	94.8	93.9	94.0
Beam width/deg	2.2	1.5	0.8	0.92	0.42	0.19
Antenna diameter/m	1.6					
Scan period/s	1.5					
Antenna offset angle/(°)	47.5					
Earth-incidence angle/(°)	55					
Orbit altitude/km	705					
Swath width/km	1,445					
Orbit type	Sun-synchronous, 98.2° inclination, 13:30 equator crossing					
Orbit period/min	98.8					
Sub-spacecraft velocity/(km·s^{-1})	6.76					

$$\boldsymbol{A}_{10\times N}=\begin{pmatrix} TB_{6.9\mathrm{H},1} & TB_{6.9\mathrm{H},2} & \cdots & TB_{6.9\mathrm{H},N} \\ TB_{6.9\mathrm{V},1} & TB_{6.9\mathrm{V},2} & \cdots & TB_{6.9\mathrm{V},N} \\ \vdots & \vdots & \ddots & \vdots \\ TB_{36.5\mathrm{V},1} & TB_{36.5\mathrm{V},2} & \cdots & TB_{36.5\mathrm{V},N} \end{pmatrix}. \quad (2)$$

Then the data matrix $\boldsymbol{A}$ can be decomposed as

$$\boldsymbol{A}=\boldsymbol{A}_1+\boldsymbol{A}_2=\sum_{i=1}^{\alpha}\vec{e}_i\vec{u}_i+\sum_{i=\alpha+1}^{10}\vec{e}_i\vec{u}_i. \quad (3)$$

The determination of integer parameter α of this research will be given later. As the PC modes are listed in the order of decreasing eigenvalue magnitude, the data matrix $\boldsymbol{A}_1$ expresses the main characteristics of brightness temperatures. The matrix $\boldsymbol{A}_2$, which is the sum of the brightness temperatures of PC modes from $(\alpha+1)^{\text{th}}$ to 10^{th}, can be defined as the residual data matrix. Therefore, $\boldsymbol{A}_1$ represents strong multichannel correlation component and the uncorrelated component with RFI signals are contained in the residual matrix $\boldsymbol{A}_2$. By choosing a suitable value of α, RFI signals become the main part of $\boldsymbol{A}_2$.

During the second step of DPCA, another PCA is applied to the residual data matrix $\boldsymbol{A}_2$. Using the method proposed by Zou et al. (2012), the vector of normalized RFI indices of $\boldsymbol{A}_2$ can be written as follows:

$$\vec{R}_{indices}^{\boldsymbol{A}_2}=\begin{pmatrix} TB_{6.9\mathrm{H}}-TB_{10.7\mathrm{H}} \\ TB_{18.7\mathrm{H}}-TB_{23.8\mathrm{H}} \\ TB_{18.7\mathrm{V}}-TB_{23.8\mathrm{V}} \\ TB_{23.8\mathrm{H}}-TB_{36.5\mathrm{H}} \\ TB_{23.8\mathrm{V}}-TB_{36.5\mathrm{V}} \end{pmatrix}. \quad (4)$$

This equation is used to identify RFI at 6.925 GHz horizontal polarization. And the RFI indices for 6.925 GHz vertical polarization can be written as

$$\vec{R}_{indices}^{\boldsymbol{A}_2}=\begin{pmatrix} TB_{6.9\mathrm{V}}-TB_{10.7\mathrm{V}} \\ TB_{18.7\mathrm{H}}-TB_{23.8\mathrm{H}} \\ TB_{18.7\mathrm{V}}-TB_{23.8\mathrm{V}} \\ TB_{23.8\mathrm{H}}-TB_{36.5\mathrm{H}} \\ TB_{23.8\mathrm{V}}-TB_{36.5\mathrm{V}} \end{pmatrix}. \quad (5)$$

The data matrix from $\vec{R}_{indices}^{\boldsymbol{A}_2}$ in Eq. (4) is defined as

$$\boldsymbol{B}_{5\times N}=\begin{pmatrix} (TB_{6.9\mathrm{H}}-TB_{10.7\mathrm{H}})_1 & (TB_{6.9\mathrm{H}}-TB_{10.7\mathrm{H}})_2 & \cdots & (TB_{6.9\mathrm{H}}-TB_{10.7\mathrm{H}})_N \\ (TB_{18.7\mathrm{H}}-TB_{23.8\mathrm{H}})_1 & (TB_{18.7\mathrm{H}}-TB_{23.8\mathrm{H}})_2 & \cdots & (TB_{18.7\mathrm{H}}-TB_{23.8\mathrm{H}})_N \\ \vdots & \vdots & \ddots & \vdots \\ (TB_{23.8\mathrm{V}}-TB_{36.5\mathrm{V}})_1 & (TB_{23.8\mathrm{V}}-TB_{36.5\mathrm{V}})_2 & \cdots & (TB_{23.8\mathrm{V}}-TB_{36.5\mathrm{V}})_N \end{pmatrix}. \quad (6)$$

Similar to the first step, we can get those eigenvalues and corresponding eigenvectors of the data matrix $\boldsymbol{B}_{5\times N}$ which can be reconstructed from the five PC modes,

$$B_R = \mathbf{EU} = \sum_{i=1}^{5} \vec{e}_i \vec{u}_i, \tag{7}$$

where $\vec{u}_i = [u_{i,1}, u_{i,2}, \ldots, u_{i,N}]$ is i^{th} PC coefficient. The first PC mode has the maximum variance. In normal conditions, brightness temperatures increase with the frequency. The existence of RFI signals at 6.925 GHz channels is the main reason for a reversed spectral gradient (brightness temperatures at 6.925 GHz higher than that at 10.7 GHz). High values of $\vec{u}_1$ indicate the presence of RFI. The higher values of $\vec{u}_1$ mean the greater probabilities of the presence of RFI.

4 Numerical results

A snowstorm weather process from January 31 to February 2, 2011 was chosen for the RFI identification experiments. This blizzard was located around the US and Canada on Groundhog Day, so it was called the 2011 Groundhog Day Blizzard. It brought cold air, heavy snowfall, blowing snow, and mixed precipitation on a path from New Mexico and northern Texas to New England and Eastern Canada. Many large cities were affected, such as St. Louis, Detroit, New York, Boston, Dallas, and Houston. Figure 1 shows the spatial distribution of the daily mean snow depth from January 31 to February 3, 2011. The data were obtained from the National Climatic Data Center of NOAA, which were collected from the National Weather Service (NWS) Cooperative Observer stations and NWS First Order stations.

Figure 2 presents the spatial distribution of AMSR-E brightness temperatures at 6.925 GHz, 10.65 GHz, and 89.0 GHz on horizontal and vertical polarizations over the United States on February 1, 2011. The brightness temperatures of the north central and northeast regions are lower than those of the south, southeast, and west coastal areas. The locations of low brightness temperatures are consistent with the positions of snow cover in Fig. 1. At the 6.925 GHz channels, there are some visible "hot spots" where brightness temperatures are higher than the surrounding area. At the 89.0 GHz channels, the differences of brightness temperatures between snow covered regions and the other regions are more obvious than other channels, and there are sharp brightness temperature gradients at the edge of snow cover.

The DPCA method is based on the fact that the natural radiation from snow surfaces affects microwave measurements at all channels while RFI only affects the measurements at low frequencies. We use this method to separate the scattering effect of snow surface and RFI signals. According to section 3, brightness temperatures are separated into high correlated part ($\boldsymbol{A}_1$) and the residual part ($\boldsymbol{A}_2$) by the first step of DPCA. Table 2 lists the variances and accumulated variances of the brightness temperatures at 6.9−36.5 GHz over the United States on February 1, 2011. The first PC mode contributes more than 99.8% of the total data variances, and the first 4 PC modes embody the vast majority of data information (accumulated variance more than 99.99%).

The spatial distributions of the $\boldsymbol{A}_1$ and $\boldsymbol{A}_2$ for 6.925 GHz horizontal and vertical polarizations are given in Fig. 3.

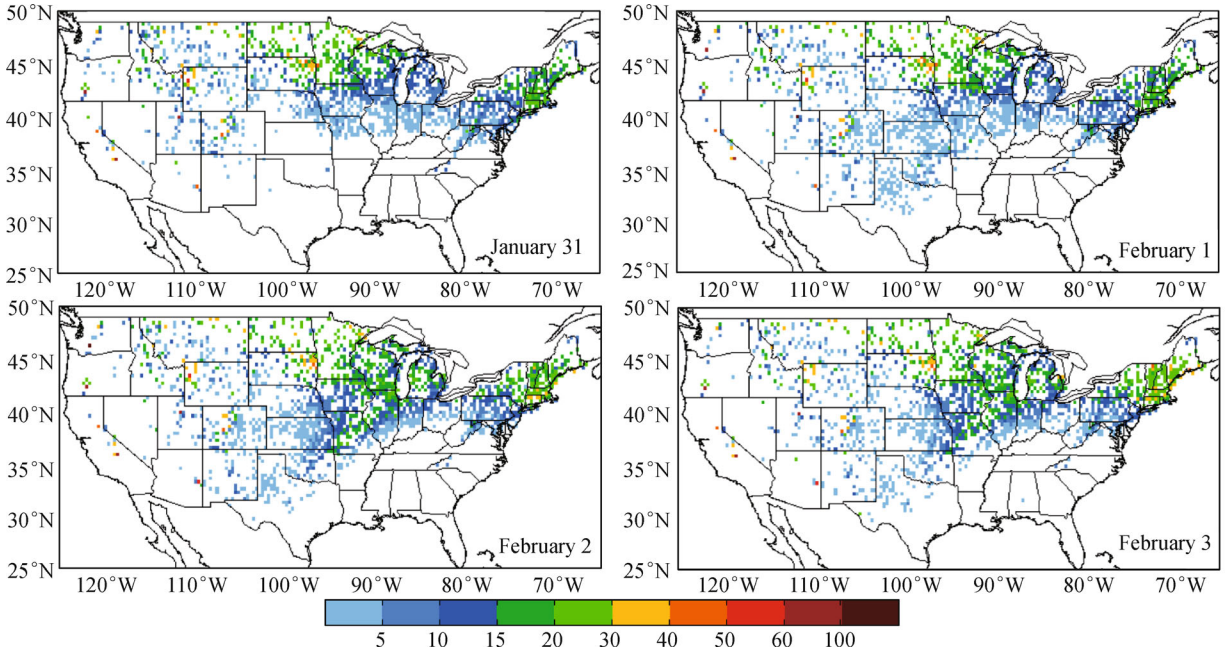

Fig. 1 Daily mean snow depth (unit: inch) from NWS stations observations during the blizzard from January 31 to February 3, 2011.

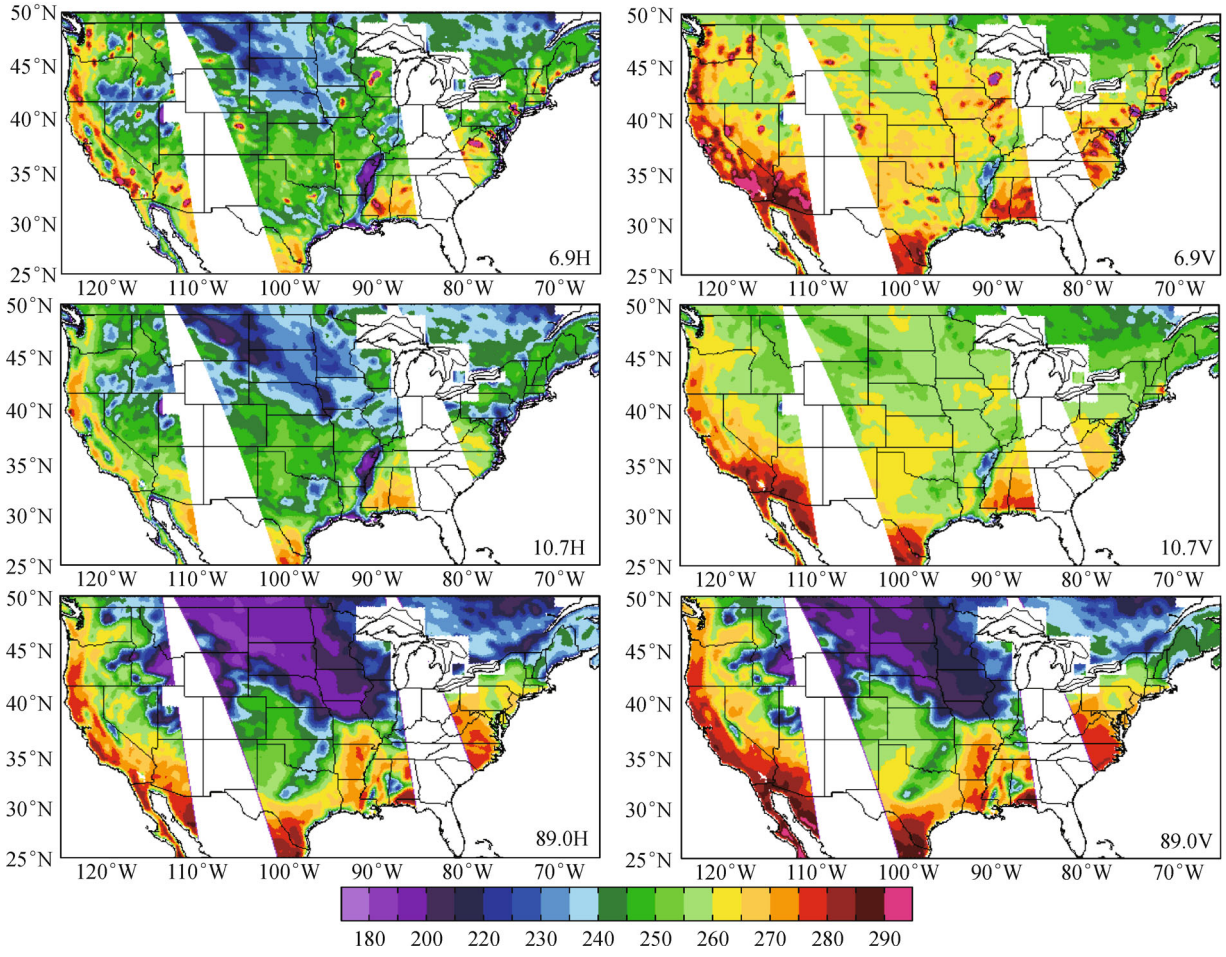

Fig. 2 Brightness temperatures at 6.925 GHz (top panels), 10.65 GHz (middle panels), and 89.0 GHz (bottom panels) on horizontal (left panels) and vertical (right panels) polarizations over the U.S. on February 1, 2011.

Table 2 Percentages of explained variances and accumulative variances for the first nine principle component (PC) modes of the brightness temperatures over the United States on February 1, 2011

PC mode number	Percentage of explained variance/%	Percentage of accumulative variance/%
1	99.89111922	99.89111922
2	0.06613443	99.95725366
3	0.02539442	99.98264808
4	0.01101284	99.99366092
5	0.00425833	99.99791926
6	0.00134824	99.99926749
7	0.00047151	99.99973900
8	0.00013511	99.99987411
9	0.00007512	99.99994923
10	0.0000004546	0.9999999469

Here α is set to 2. In $\boldsymbol{A}_1$ fields, the low brightness temperatures caused by snow mainly appeared in the middle and northeast area. The spatial distributions of brightness temperatures at horizontal and vertical polarization are very similar, but the brightness temperatures of horizontal polarization are lower than those of vertical polarization. In the $\boldsymbol{A}_2$ part, there are many small scale features while the brightness temperatures in $\boldsymbol{A}_1$ are much smoother. Comparing these two parts, it is believed that the "hot spots" caused by RFI (Li L et al., 2004) are separated into the $\boldsymbol{A}_2$ fields.

The second step of the DPCA method was applied to the $\boldsymbol{A}_2$ field. In order to show the impact of α, the variations of the first PC coefficient with respect to α over some regions are shown in Fig. 4. Earlier researches indicated that RFI is usually located near large cities (Li et al., 2004; Njoku et al., 2005; Wu and Weng, 2011), so five areas were chosen near the following big cities: Boston, St Louis, Denver, Dallas, and Los Angeles. Figure 4 shows the variation of the first PC coefficients with respect to α from the second step of DPCA in the five selected regions shown in Fig. 5 (a). As the larger value of the first PC coefficient suggests the higher probability of the presence of RFI signals, the value of α with the largest first PC coefficient should be chosen. From Fig. 4, we found that the PC coefficient increases significantly when α changes from 1 to 2, and the

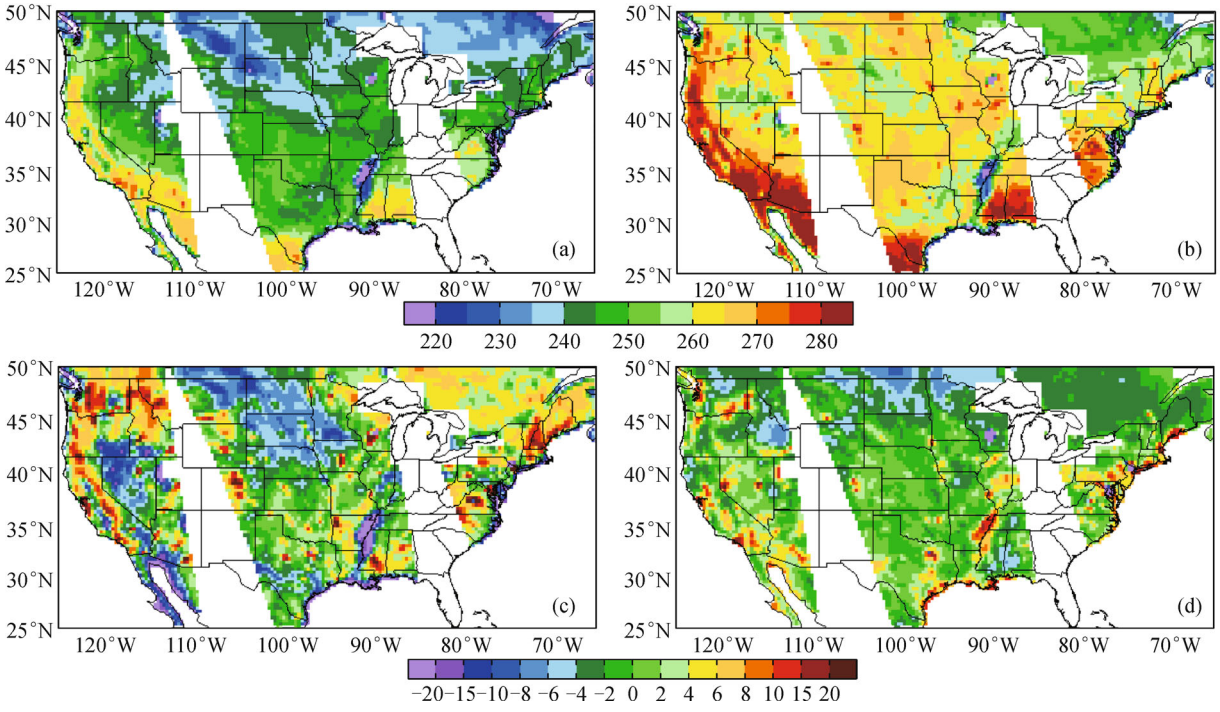

Fig. 3 Brightness temperatures of 6.925 GHz from 10 channels on horizontal (left panels) and vertical (right panels) polarizations reconstructed $\boldsymbol{A}_1$ ((a) and (b)), $\boldsymbol{A}_2$ ((c) and (d)) with $\alpha = 2$ on February 1, 2011.

PC coefficient with $\alpha = 2$ is very close to $\alpha = 3$. Because the smaller α takes, the more brightness temperature (including RFI signals) information is embodied in residual part $\boldsymbol{A}_2$. So, choosing $\alpha = 2$ can ensure as much information of RFI as possible will be separated.

Figure 5 shows the distributions of RFI signals at 6.925 GHz over the United States on February 1, 2011 when α is set to 2. Here data points with larger values indicate the presence of stronger RFI signals. The locations of 6.925 GHz RFI signals are almost the same for horizontal and vertical polarizations. RFI for horizontal polarization is stronger than that for vertical polarization.

The results from PCA, NPCA, and DPCA for AMSR-E data on February 1, 2011 (with snow cover) and data during April 1−30, 2011 (non-snow period) are compared in Fig. 6. Both of the PCA and NPCA methods use the RFI indices from the original brightness temperatures (Zou et al., 2012) while DPCA uses the indices from the reconstructed brightness temperatures. As the RFI signals persist in time, the results of snow period and non-snow period should be consistent. Figure 6 shows that the PCA method cannot detect RFI over snow covered regions. There is a large area of positive values in the high latitudes. The NPCA method can identify RFI, but the detected RFI signals are significantly weaker over snow covered regions. The results from the DPCA method are very

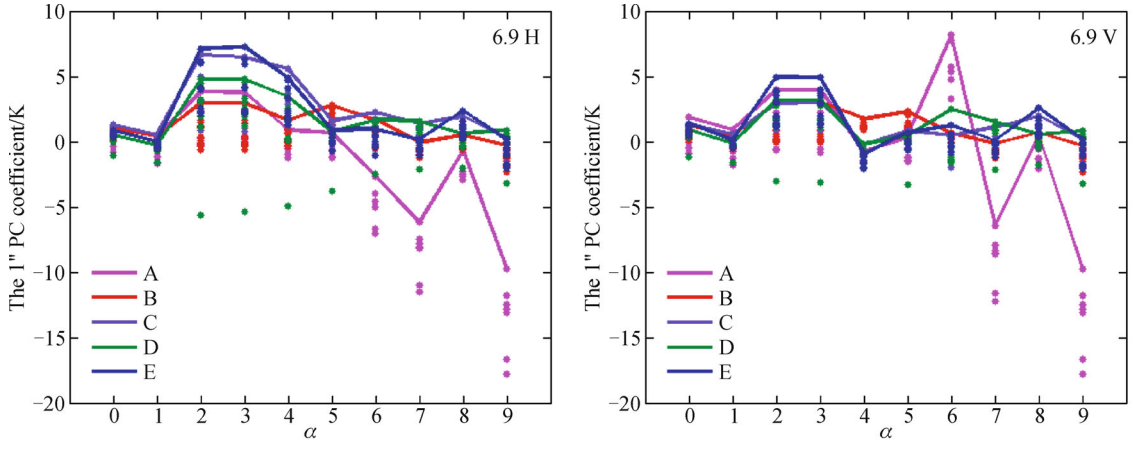

Fig. 4 Variation of the first PC coefficients with respect to α for RFI detection of 6.9 GHz horizontal (left panel) and vertical (right panel) polarizations at all grid points in the boxes A (magenta), B (red), C (purple), D (green), and E (blue) indicated in Fig. 5.

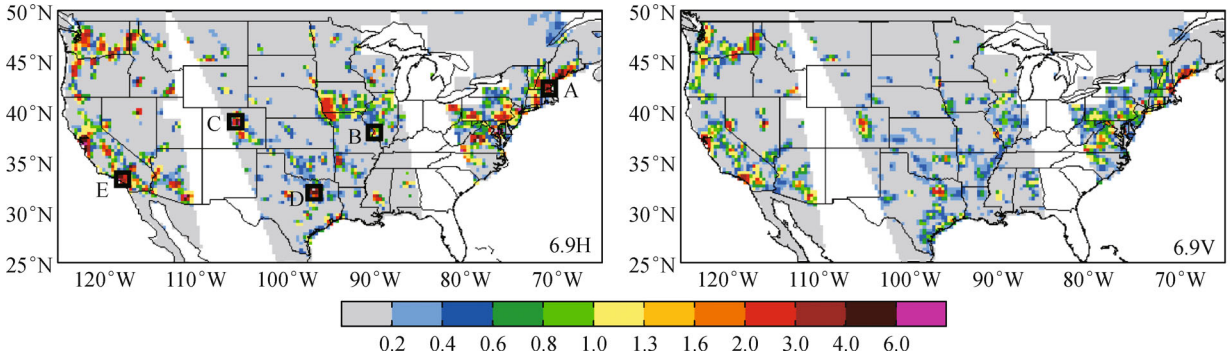

Fig. 5 RFI distributions of 6.925 GHz at horizontal (a) and vertical (b) polarizations identified by the DPCA method over the United States on February 1, 2011.

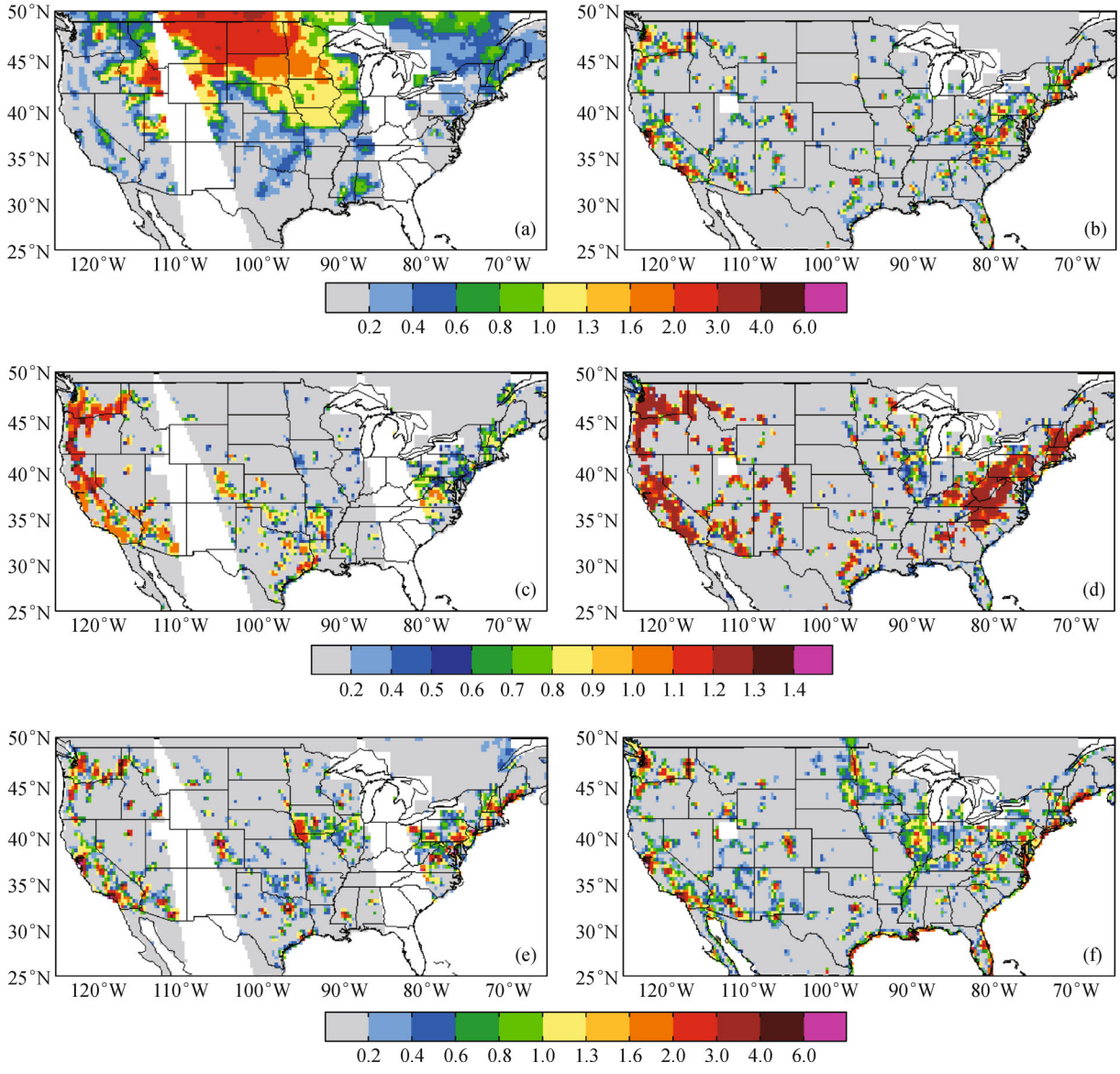

Fig. 6 RFI distributions of 6.925 GHz at horizontal polarization identified by the PCA (a, b), NPCA (c, d) and DPCA (e, f) method over the United States on February 1, 2011 (left panels) and during April 1−30, 2011 (right panels).

consistent no matter whether there is snow cover or not. It can be concluded that the DPCA method can avoid the influence of snow scattering on identifying RFI signals in AMSR-E data.

Figure 7 presents the RFI detected by DPCA from January 31 to February 3, 2011, on each day of the blizzard period. It can be found that the results are very similar. Although snow coverage on each day is different (Fig. 1), the spatial distribution of RFI detected by the DPCA method is very consistent.

The DPCA method was also applied to other different seasons, and the results are shown in Fig. 8. January, April, July, and October are chosen as typical months for each season. From these figures, it can be found that the distribution of RFI signals in different seasons are almost the same, indicating RFI persist in time.

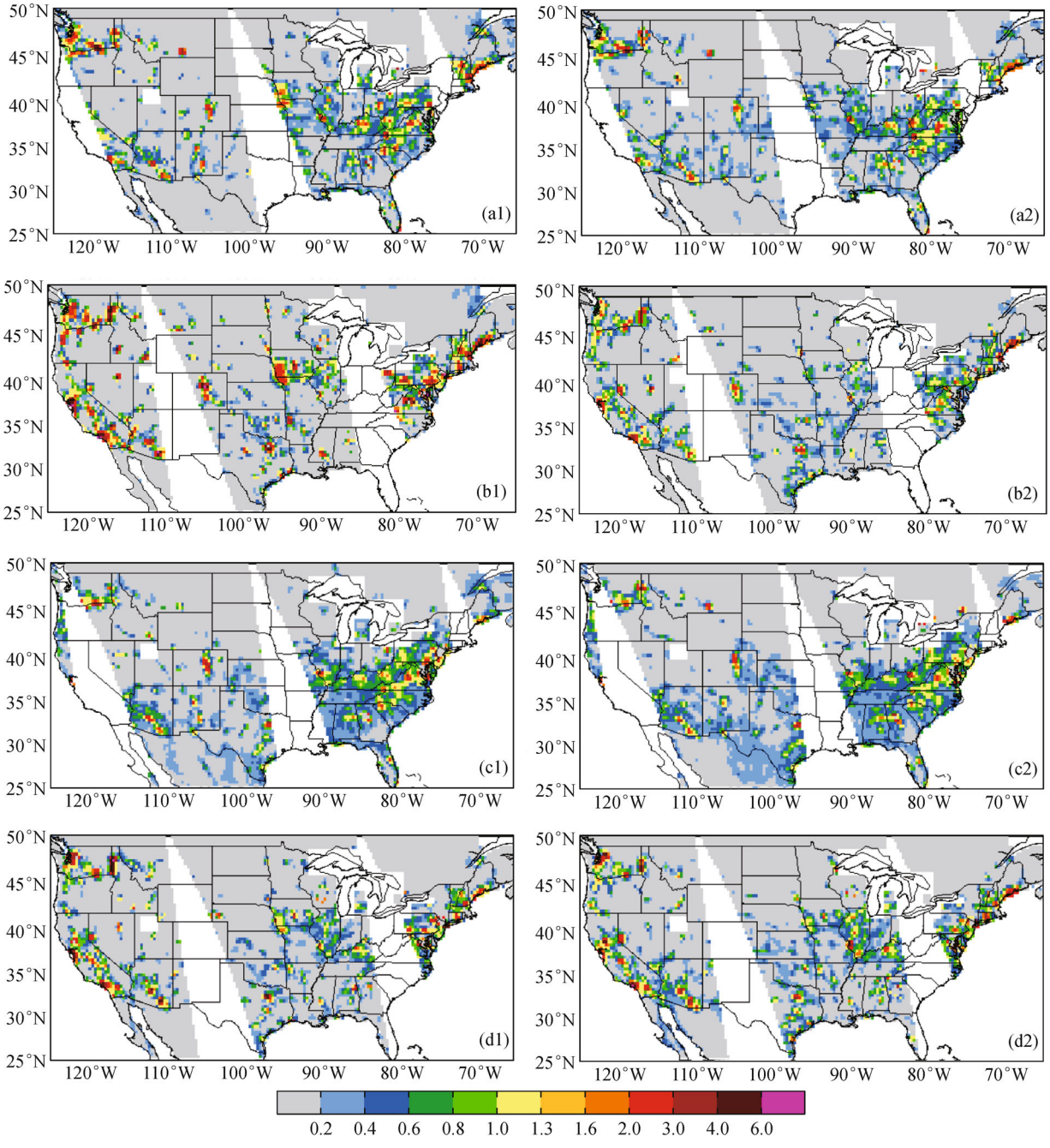

Fig. 7 RFI distributions of 6.925 GHz at horizontal (left panels) and vertical (right panels) polarization identified by the DPCA method over the United States on (a1, a2) January 31, (b1, b2) February 1, (c1,c2) February 2, and (d1, d2) February 3, 2011.

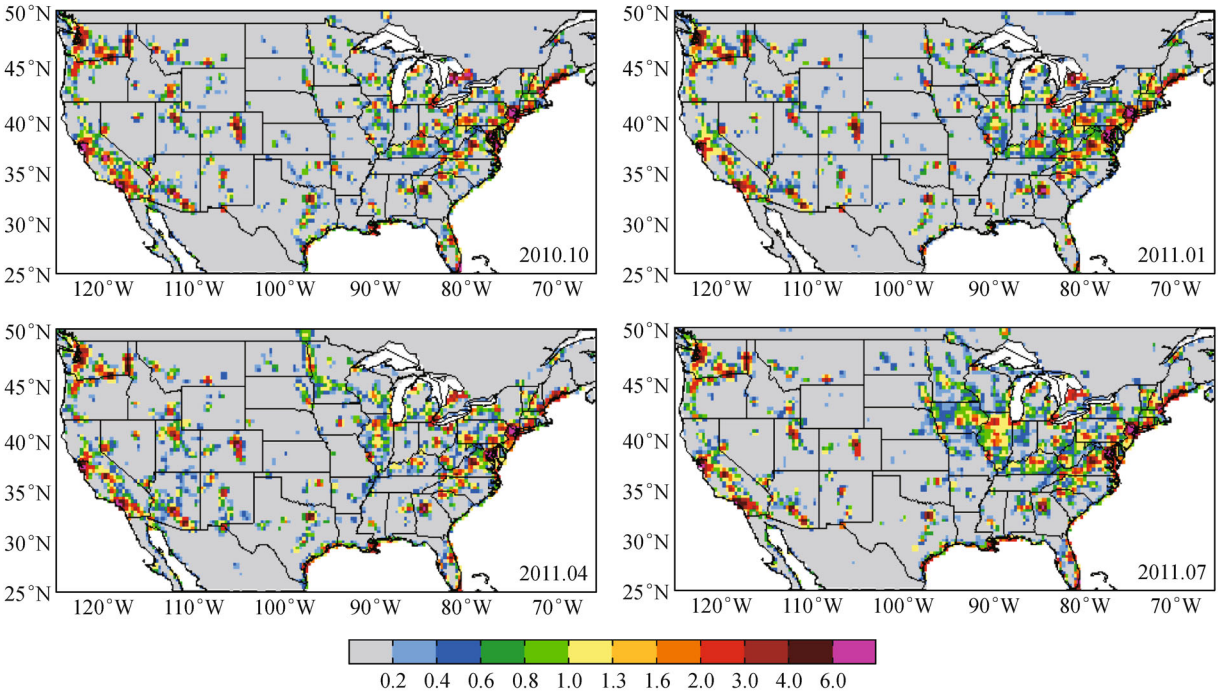

Fig. 8 RFI distributions of 6.925 GHz at horizontal polarization identified by the DPCA method over the United States during October 1−31, 2010, January 1−31, April 1−30, and July 1−31, 2011.

5 Summary and conclusions

RFI signals usually appear at the low frequency channels of microwave radiometer. It is very important to detect RFI before the contaminated data is used in retrievals or data assimilation. When the RFI signals are located over a surface covered by snow, it is difficult to identify them. In this paper, the double principal component analysis (DPCA) method is adopted to investigate the detection of RFI over snow covered regions during a blizzard weather process.

Taking advantage of the correlation of different channels for natural and snow radiations, and the de-correlation caused by RFI, DPCA can separate RFI signals from weather signals clearly. Results show that the PCA method cannot detect RFI over snow covered surfaces. The NPCA method can identify RFI signals, but RFI is significantly weaker with the presence of snow cover. The DPCA method can avoid the influence of snow scattering. The results from the DPCA method are very consistent no matter whether there is snow or not. For different distributions of snow cover, the RFI signals detected by DPCA are almost the same. For different seasons, the detection results are also consistent. Therefore, it can be considered that the DPCA method is effective to identify RFI signals in the areas covered by snow.

Since the selection of parameters is not completely objective and automatic in this research, further study will be needed. More tests on the feasibility of the DPCA method in other conditions are also required.

Acknowledgements This work was supported jointly by China Special Fund for Meteorological Research in the Public Interest (No. GYHY-201406008), the Research innovation Program for college graduates of Jiangsu Province (CXLX13_483), and the Priority Academic Program Development (PAPD) of Jiangsu Higher Education Institutions.

References

Ashcroft P, Wentz F (2000). Algorithm theoretical basis document, AMSR Level 2A algorithm. RSS Tech. Report 121599B-1

Ellingson S W, Johnson J T (2006). A polarimetric survey of radio-frequency interference in C- and X-bands in the continental United States using WindSat radiometry. IEEE Trans Geosci Rem Sens, 44 (3): 540–548

Imaoka K, Sezai T, Takeshima T, Kawanishi T, Shibata A (2002). Instrument characteristics and calibration of AMSR and AMSR-E. Geoscience and Remote Sensing Symposium, 1: 18–20

Kawanishi T, Sezai T, Ito Y, Imaoka K, Takeshima T, Ishido Y, Shibata A, Miura M, Inahata H, Spencer R W (2003). The advanced microwave scanning radiometer for the earth observing system (AMSR-E), NASDA's contribution to the EOS for global energy and water cycle studies. IEEE Trans Geosci Rem Sens, 41(2): 184–194

Kelly R E, Chang A T, Tsang L, Foster J L (2003). A prototype AMSR-E global snow area and snow depth algorithm. IEEE Trans Geosci Rem Sens, 41(2): 230–242

Lacava T, Coviello I, Faruolo M, Mazzeo G, Pergola N, Tramutoli V (2013). A multitemporal Investigation of AMSR-E C-band radio-frequency interference. IEEE Trans Geosci Rem Sens, 51(4): 2007–2015

Li L, Gaiser P W, Bettenhausen M, Johnston W (2006). WindSat radio-frequency interference signature and its identification over land and ocean. IEEE Trans Geosci Rem Sens, 44(3): 530–539

Li L, Njoku E G, Im E, Chang P, Germain K S (2004). A preliminary survey of radio-frequency interference over the U.S. in Aqua AMSR-E data. IEEE Trans Geosci Rem Sens, 42(2): 380–390

McKague D, Puckett J J, Ruf C (2010). Characterization of K-band radio frequency interference from AMSR-E, WindSat and SSM/I. In: Proc. IGARSS: 2492–2494

Njoku E G, Ashcroft P, Chan T K, Li L (2005). Global survey and statistics of radio-frequency interference in AMSR-E land observations. IEEE Trans Geosci Rem Sens, 43(5): 938–947

Njoku E G, Jackson T J, Lakshmi V, Chan T K, Nghiem S V (2003). Soil moisture retrieval from AMSR-E. IEEE Trans Geosci Remote Sens, 41(2): 215–229

Njoku E G, Koike T, Jackson T, Paloscia S (2000). Retrieval of soil moisture from AMSR data. In: Pampaloni P, Paloscia S, eds. Microwave Radiometry for Remote Sensing of the Earth's Surface and Atmosphere. Utrecht: VSP, 525–533

Njoku E G, Li L (1999). Retrieval of land surface parameters using passive microwave measurements at 6−18 GHz. IEEE Trans Geosci Rem Sens, 37(1): 79–93

Owe M, De Jeu R, Walker J (2001). A methodology for surface soil moisture and vegetation optical depth retrieval using the microwave polarization difference index. IEEE Trans Geosci Rem Sens, 39(8): 1643–1654

Parkinson C L, Chahine M T, Kummerow C D, Alomonson V V S (2003). Aqua: an earth-observing satellite mission to examine water and other climate variables. IEEE Trans Geosci Rem Sens, 41: 172–183

Shibata A, Imaoka K, Koike T (2003). AMSR/AMSR-E level 2 and 3 algorithm developments and data validation plans of NASDA. IEEE Trans Geosci Rem Sens, 41(2): 195–203

Wilheit T, Kummerow C D, Ferraro R (2003). Rainfall algorithms for AMSR-E. IEEE Trans Geosci Remote Sens, 41(2): 204–214

Wu Y, Weng F Z (2011). Detection and correction of AMSR-E radio-frequency interference (RFI). Acta Meteor Sinica, 25(5): 669–681

Zhao J, Zou X L, Weng F Z (2013). WindSat radio-frequency interference signature and its identification over Greenland and Antarctic. IEEE Trans Geosci Remote Sens, 51(9): 1–10

Zou X L, Zhao J, Weng F Z, Qin Z K (2012). Detection of radio-frequency interference signal over land from FY-3B Microwave Radiation Imager (MWRI). IEEE Trans Geosci Rem Sens, 50(12): 4994–5003